

PAPER • OPEN ACCESS

Numerical study of divertor detachment in TCV H-mode scenarios


To cite this article: H Yang *et al* 2023 *Plasma Phys. Control. Fusion* **65** 125005

View the [article online](#) for updates and enhancements.

You may also like

- [Parameter dependencies of the separatrix density in low triangularity L-mode and H-mode JET-ILW plasmas](#)
B. Lomanowski, G. Rubino, A. Uccello et al.
- [Power exhaust and core-divertor compatibility of the baffled snowflake divertor in TCV](#)
S Gorno, C Colandrea, O Février et al.
- [Overview of the TCV tokamak experimental programme](#)
H. Reimerdes, M. Agostini, E. Alessi et al.

Numerical study of divertor detachment in TCV H-mode scenarios

H Yang^{1,*} , G Ciraolo¹, O Février² , D Galassi² , J Bucalossi¹, H Bufferand¹, S Gorno² , S Henderson³ , H Reimerdes² , C Theiler² , F Bagnato², G Falchetto¹, N Fedorczak¹, N Rivals¹ , P Tamain¹ and the TCV Team⁴

¹ CEA, IRFM, F-13108 Saint Paul-lez-Durance, France

² Ecole Polytechnique Fédérale de Lausanne (EPFL), Swiss Plasma Center (SPC), Lausanne, Switzerland

³ United Kingdom Atomic Energy Authority, Culham Science Centre, Abingdon, Oxon OX14 3DB, United Kingdom

E-mail: hao.yang@etu.univ-amu.fr

Received 1 August 2023, revised 9 October 2023

Accepted for publication 25 October 2023

Published 2 November 2023



Abstract

The effect of divertor closure and nitrogen seeding on the detachment process has been studied by performing 2D numerical simulations of tokamak à configuration variable (TCV) H-mode divertor scenarios with the SOLEDGE3X-EIRENE edge plasma transport code. The simulations reveal that, in the cases with only deuterium gas fuelling, detachment occurs at a similar level of divertor neutral pressure (≈ 0.76 Pa), despite the difference in divertor closure achieved by changing the length of the outer baffle. Nitrogen reduces the target temperature with little effect on the upstream density and momentum loss but drops the upstream pressure, leading to a decrease in the target particle flux and divertor neutral pressure. Furthermore, when the radiation front starts to move up from the outer target, the peak parallel heat flux level at the outer target remains approximately the same (≈ 2.3 MW m⁻²), regardless of whether it is a deuterium fuelling scan, a nitrogen seeding scan at a fixed fuelling rate, or a change in the length of the outer baffle. An empirical partial detachment qualifier calibrated on AUG experimental data was compared with the TCV simulations. The results show good agreement in detachment state prediction, indicating the potential of this detachment qualifier to be applied in devices of different sizes, emphasizing the combined influence of input power entering the divertor, neutral pressure, and the concentration and species of impurity in achieving divertor detachment.

Keywords: plasma physics, H-mode, numerical modelling, divertor closure, nitrogen seeding, detachment

(Some figures may appear in colour only in the online journal)

⁴ See Reimerdes *et al* 2022 (<https://doi.org/10.1088/1741-4326/ac369b>) for the TCV Team.

* Author to whom any correspondence should be addressed.



Original Content from this work may be used under the terms of the [Creative Commons Attribution 4.0 licence](https://creativecommons.org/licenses/by/4.0/). Any further distribution of this work must maintain attribution to the author(s) and the title of the work, journal citation and DOI.

1. Introduction

In future tokamaks like ITER and DEMO [1, 2], a high level of heating power leaves the confined region and enters into the *scrape-off-layer* (SOL), ultimately depositing particles and heat onto a relatively narrow surface of the divertor target. If unmitigated, this heat flux can exceed the wall material limitation, which for ITER is approximately 10 MW m^{-2} [1]. Detached divertor plasmas are considered an effective solution for reducing target heat flux and minimizing target erosion. The divertor keeps plasma-wall interaction at a distance from the main plasma and reduces the impact of impurities on the core region. Radiation from the impurity and hydrogen species and plasma recombination can occur at a distance from the divertor target, spreading most of the heat loading (about 60%–75% in ITER and more than 95% in DEMO [3]) over a larger surface, thus keeping the peak heat flux at the target at a manageable level. Such operating regimes are called ‘divertor detachment’. Detachment is characterised by the appearance of large gradients in total plasma pressure (static plus dynamic) parallel to the magnetic field [4]. It can be achieved by either raising the core plasma density, injecting impurities, or lowering the power entering the divertor. However, strongly detached divertor plasmas can extend into the closed field line plasma near the X-point and seriously degrade core plasma confinement [5]. There are scenarios where the radiative cooling is limited to the X-point region, without detriment to core performance [6]. The desired state for long discharge operation requires compatibility between divertor detachment and core performance.

For high power, high confinement operations, impurities (such as N_2 , Ne, Ar, Kr, Xe) will be necessary to achieve detachment [7, 8]. Nitrogen is often used to induce detachment in present experiments, as it primarily radiates in the SOL and divertor region in medium-sized tokamaks such as *tokamak à configuration variable* (TCV) [9]. The radiated power increases significantly and the target heat load is largely reduced with nitrogen seeding [7]. We note here that, due to the chemical reactivity of nitrogen, it can react with the deuterium and tritium, forming ammonia, which is a concern for ITER due to tritium retention, and therefore poses operational challenges [10]. Nonetheless, in medium-sized tokamaks not operating tritium, nitrogen remains an interesting species to study impurity-driven detachment, thanks to its radiative properties.

Extensive investigations of divertor detachment with and without nitrogen seeding in *Low-confinement mode* (L-mode) [7] and *High-confinement mode* (H-mode) [11] have been performed by the TCV [12]. TCV has great flexibility in plasma shaping, and the divertor closure can be varied from one experimental campaign to the next by installing baffles of different lengths [13]. The impact of divertor closure has been investigated experimentally and numerically in TCV, indicating that baffles strongly increase the neutral pressure in the divertor, and facilitate access to a colder divertor, promoting

detachment at a lower core plasma density threshold [14–18]. This result is consistent with studies of divertor closure in multiple tokamak devices such as DIII-D [19–25], ASDEX-Upgrade [26], JET [27–29], EAST [30, 31], JT-60U [32], and WEST [33].

The present work focuses on the numerical modelling of H-mode TCV plasmas and studies the impact of divertor closure and nitrogen seeding on the detachment process. The simulations employed the SOLEDGE3X code in 2D transport mode [34, 35]. The multi-species plasma fluid model is derived using the approach by Zhdanov [36]. A separate parallel momentum balance equation is solved for every single ionization state. Temperatures are also separated. SOLEDGE3X is coupled with EIRENE to handle kinetic neutrals. It inherits the specific characteristics of SOLEDGE2D, which enable simulations of the plasma up to the wall. This is achieved by using an immersed boundary method to drive Bohm boundary conditions at the interface between the plasma and solid surfaces. This capability allows the code to handle flexible wall geometries, such as divertor baffles [37].

This paper is organized as follows: in section 2, we present the simulation setup of the base case, comparing the simulation results against experimental data. In section 3, an upstream separatrix density scan is performed to explore divertor regimes from attached to detached, based on the validated base case. We evaluate the movement of the peak radiation region qualitatively using the radiation front height. In section 4, the impact of divertor closure is investigated by comparing cases with long and short baffles. In section 5, nitrogen seeding is introduced in the simulation and the impact of nitrogen on the plasma, momentum loss, power radiation, and detachment is investigated. In section 6, a simplified partial detachment prediction model is presented and compared with the TCV simulation. The conclusion is presented in section 7.

2. Reference simulation setup and results

To investigate the properties of H-mode plasmas with repetitive *edge localized modes* (ELMs), the TCV discharge #70 690, a typical type-I ELMy H-mode, was selected as the experimental reference. The operational parameters are shown in table 1. The discharge was performed in a *lower-single-null* (LSN) magnetic configuration, and the wall geometry is shown in figure 1. The D_2 gas fuelling was injected near the outer separatrix at the outer target, and the N_2 seeding was injected in the *private flux region* (PFR). The recycling coefficient of deuterium on the entire wall is set to 0.99 which yields reasonable gas puff levels with respect to experiments [15]. The recycling coefficient of nitrogen is estimated to range from 0.3 to 0.5, based on spectroscopic measurements and previous TCV L-mode simulations with N_2 seeding [38]. The recycling coefficient of carbon lies within the same range to obtain a reasonable radiated power in the SOL [16]. Here, the recycling

Table 1. The operational parameters of TCV discharge #70690 at $t = 1$ s. The total heating power P_{in}^{exp} , computed using the ASTRA code [42], represents the power delivered to the core plasma from Ohmic heating and *Neutral-Beam Injection* (NBI). Core radiated power $P_{rad,core}^{exp}$ represents the radiation inside the *Core-Edge-Interface* (CEI) (figure 1) at normalized poloidal magnetic flux coordinate $\psi_N = (\psi - \psi_0)/(\psi_{sep} - \psi_0) = 0.75$, with ψ the poloidal magnetic flux and ψ_0 and ψ_{sep} the poloidal magnetic flux at the magnetic axis and at the separatrix, respectively.

| | |
|---|--------|
| Major radius R_0 (m) | 0.89 |
| Minor radius a (m) | 0.25 |
| Plasma current I_p (MA) | 0.21 |
| Toroidal field B_t (T) at R_0 | 1.39 |
| Total heating power P_{in}^{exp} (kW) | 510 |
| Core radiated power $P_{rad,core}^{exp}$ (kW) | 80 |
| Main impurity | Carbon |

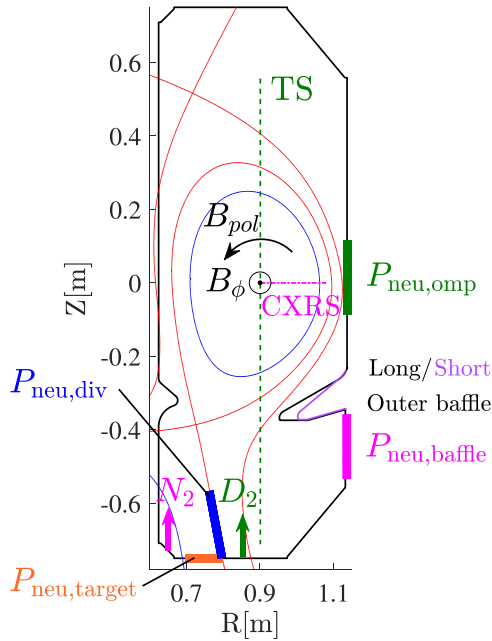


Figure 1. TCV LSN magnetic configuration (#70690 at $t = 1$ s), with wall geometries (long and short outer baffle) in a poloidal cross-section. The black solid line represents the graphite wall, the red solid curves represent the first and second separatrices, the blue circle represents the CEI, the green arrow represents the deuterium gas puff position ($R = 0.88$ m), the magenta arrow represents the nitrogen seeding position ($R = 0.65$ m). The line averaged neutral pressure P_{neu} is measured at the positions near *Outer Mid-Plane* (OMP), baffle, divertor, and target. The $P_{neu,div}$ covers the lower part of the outer divertor leg, where neutral pressure builds up when achieving detachment. The $P_{neu,div}$ is unavailable in the experimental measurements. The green dashed line corresponds to the measurement position of the *Thomson Scattering* (TS) system. The magenta dashed-dotted line corresponds to the position of the *charge eXchange recombination spectroscopy* (CXRS) diagnostic.

coefficients of nitrogen and carbon were set to 0.5. All charge states of nitrogen and carbon are considered in the simulations. However, we start this section by considering a case without

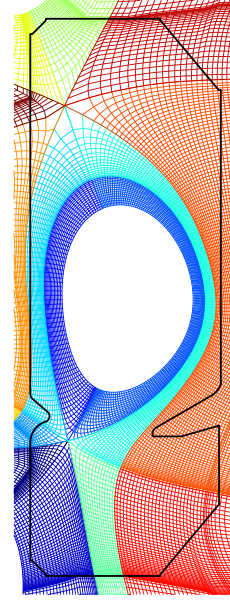


Figure 2. SOLEDGE mesh grid based on magnetic configuration of #70690 at $t = 1$ s in TCV. Domain decomposition is used to handle complex magnetic configurations such as closed and open field lines and private flux.

nitrogen seeding, and carbon is therefore the only impurity that is simulated. The physical (chemical) sputtering is estimated through the Bohdansky (Roth) model [39] in EIRENE with the plasma background provided by SOLEDGE. No molecular chemistry for carbon. The used neutral model in EIRENE includes *charge eXchange* (CX) reactions between an ionized species and its corresponding neutrals, but it does not consider cross-element CX reactions, *molecular activated recombination* (MAR), and elastic collisions with neutrals. When target temperature $T_{e,t}$ falls from 3 eV to 1 eV, MAR is found to account for up to half of the reduction of target ion particle flux on TCV during density ramps [40]. When $T_{e,t}$ falls below 1 eV, the ion-molecule ($D^+ - D_2$) elastic collisions are necessary for further heat dissipation and access to strongly recombining conditions in the fuelling scan [41]. The mesh used in the simulation is shown in figure 2.

TS measurements [43] of upstream electron density and temperature profiles, and CXRS measurements [44] of the upstream ion temperature profile are shown in figure 3. The TS measurements yield an upstream separatrix electron density, $n_{e,sep} \approx 1.36 \times 10^{19} \text{ m}^{-3}$. In the simulations, $n_{e,sep}$ is controlled by feedback adjustments of the D_2 gas puff rate to match the experimental value. We measured $T_e \approx 405$ eV at the CEI. T_i , despite the relatively large experimental uncertainties, lies within the same range as T_e . Therefore, $T_{e,CEI} = T_{i,CEI} = 405$ eV was set as the simulation temperature boundary condition.

The setup of transport coefficients in the radial direction is critical in representing the confinement properties of H-mode edge plasmas. However, calculating the transport coefficients

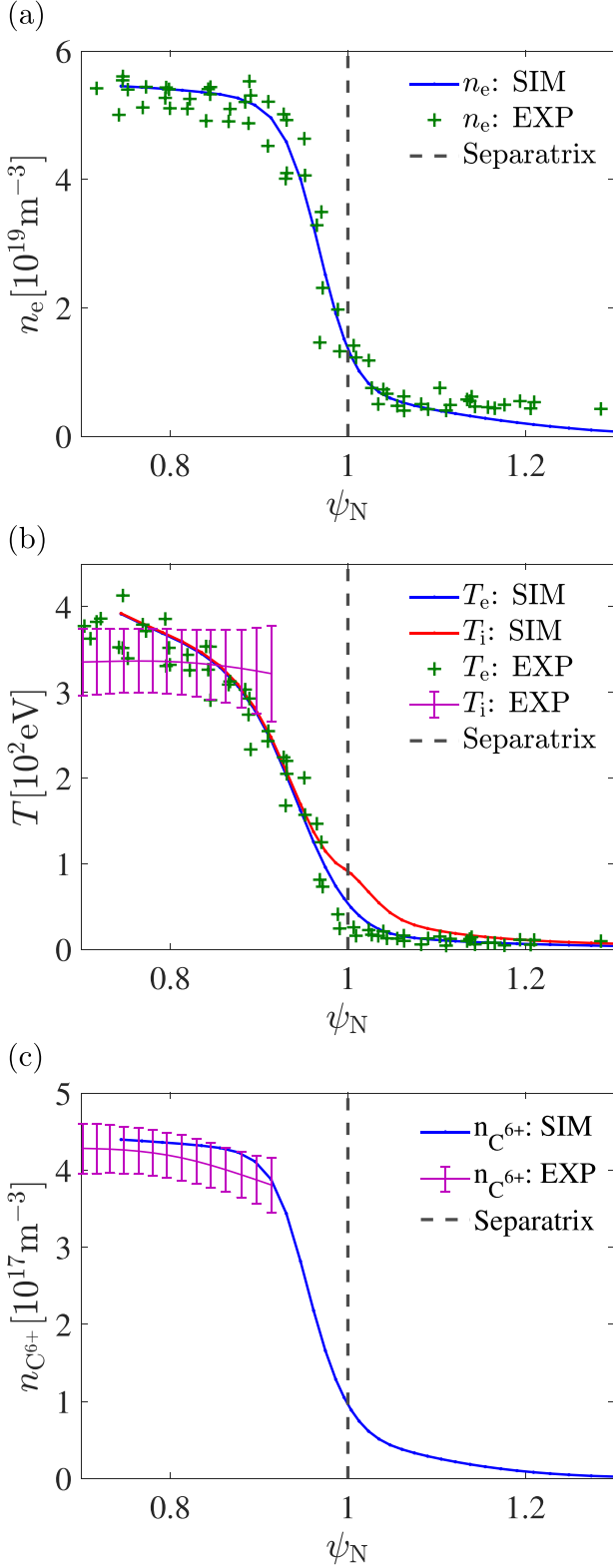


Figure 3. Radial profiles of (a) electron density, (b) temperature, and (c) C^{6+} density at the OMP, comparing the experimental measurements of n_e and T_e (raw data measured by TS, represented by the green plus sign), as well as T_i and $n_{C^{6+}}$ (measured by CXRS, raw data fitted with a spline and represented by the purple curve with error bars showing uncertainties of the fit) with the SOLEDGE-EIRENE simulation (blue and red curves). The dashed line represents the position of the separatrix.

from first-principle approaches is not straightforward, and they are usually obtained from the experimental measurements. For this simulation work, we used profile feedback control, which can automatically adjust the transport coefficients at each radial position to control the radial profiles at the OMP and match them with the experimental inter-ELMs profiles. This allows us to extract edge transport coefficients from experimental data. Since we have the experimental upstream n_e and T_e profiles (figures 3(a) and (b)), the cross-field mass diffusivity D_\perp and the radial heat flux diffusivity for electrons $\chi_{\perp,e}$ are computed separately. The experimental data from several machines (figure 7 in [45]) show that the ion-to-electron temperature ratio $\tau = T_i/T_e$ increases with radius, with $\tau = 1 \rightarrow 2.5$ in the edge plasma ($0.64 < \psi_N < 1$). To reproduce a τ profile coarsely matched with experiment, the simulation assumes the radial heat flux diffusivity for ions $\chi_{\perp,i} = 2\chi_{\perp,e}$ inside the separatrix, $\chi_{\perp,i} = \chi_{\perp,e}$ outside the separatrix. The viscosity is assumed to be constant at $\nu_\perp = 0.2 \text{ m}^2 \text{ s}^{-1}$. The transport coefficients for impurity ions are set equal to the main ions. After determining the transport coefficients at the OMP, we propagate them to the whole simulation domain. To obtain a better description of the diffusivities in 2D, we introduce the so-called ballooning transport, which enhances perpendicular transport in the vicinity of the OMP as observed in experiments [46, 47], and investigated in some modelling works [48–50]. In our simulations, the ballooning effect is described by rescaling 2D transport coefficients using equation (1) [51].

$$D_{\perp,\text{local}} = D_{\perp,\text{omp}} \left(\frac{B_{\text{omp}}}{B_{\text{local}}} \right)^b, \quad (1)$$

where D_\perp is the radial transport coefficient and B is the total magnetic field strength. We use the subscript ‘omp’ to indicate that it is a variable obtained at the OMP at a given flux surface ψ_N , and use the subscript ‘local’ to indicate that it is a variable obtained at the local poloidal position, at that same poloidal flux surface. To calculate the transport coefficients for the location inside the PFR, $D_{\perp,\text{omp}}$ is replaced by $D_{\perp,\text{sep}}$. b represents the ballooning exponent. However, directly applying this diffusivity map to simulations results in a peak target density overestimation by a factor of about 2 compared with the experimental value in the TCV case. This overestimation is not directly caused by the introduction of ballooning transport, but rather due to the competition of particle and heat transport between parallel and perpendicular parts in the divertor volume [52]. To address this, we enhanced the diffusivities by a factor of 10 in the divertor region, leading to the target profiles (density, heat flux) approximately consistent with experimental data, similarly to what was done in [53, 54]. Another approach that is not discussed in this paper would be to increase the impurity level, either through the sputtering source or by artificially increasing the radiated power, in order to achieve a better match between the simulation and the experimental results regarding the radiated power. This addresses the radiation shortfall identified in simulations [55]. Based on the enhancement of diffusivities in the divertor, the

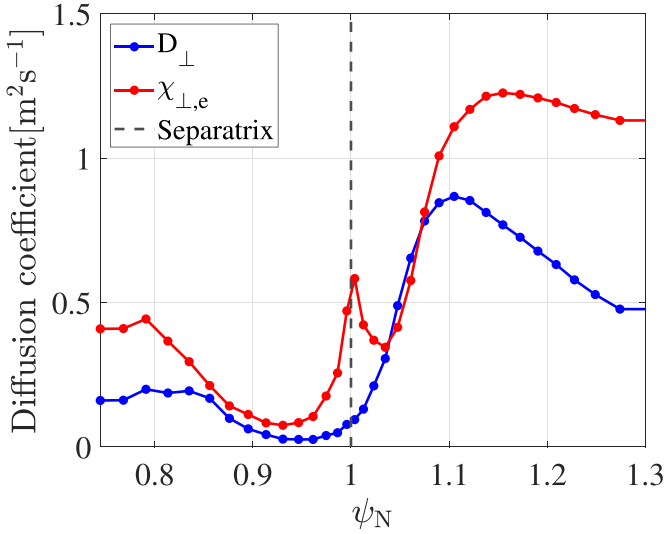


Figure 4. Profiles of D_{\perp} and $\chi_{\perp,e}$ as a function of ψ_N at the OMP, controlled by the feedback function to match the experimental density and temperature profile.

ballooning exponent b was scanned from 0 to 3, showing that different b values can impact the peak temperature and integral particle flux at the targets. A higher value of b results in a lower peak temperature at the inner target and a higher peak temperature at the outer target. Additionally, it leads to a narrower width while maintaining a similar peak particle flux at both targets. These effects have an impact on the carbon sputtering rate. A value $b = 1$ was found to result in a good match between the experiment and simulation with respect to the C^{6+} density at the OMP, as shown in figure 3(c).

To find the diffusivities that lead to the closest match between simulated and experimental OMP profiles, we first take H-mode like non-constant diffusivities at the OMP [56] to make the initial diffusion map and perform an initial simulation. Then, employing the profile feedback control process, we finally obtain the diffusivity profiles at the OMP, as shown in figure 4.

L-mode experiments have demonstrated that drifts mainly affect the plasma state at the inner target, with detachment being more easily achieved in the presence of favorable magnetic field (the direction of ion ∇B drift points downwards in the LSN magnetic configuration) compared to the unfavorable one (reversed ∇B direction) [7, 57]. Although drifts were not activated in the H-mode simulations due to the challenge in convergence with low diffusion coefficients, drifts (particularly $\mathbf{E} \times \mathbf{B}$ drift) would improve the agreement by displacing the density peak at the outer target towards the PFR. The $\mathbf{E} \times \mathbf{B}$ drift is responsible for notable cross-field transport in the divertor region, pointing from the outer SOL into the main plasma (and into the private plasma below the X-point) in the favorable magnetic field [51].

The simulation focuses on inter-ELMs condition and finds the total heating power going to the SOL is $P_{\text{in,edge}}^{\text{sim}} = 210$ kW by setting the $T_{e,\text{CEI}} = T_{i,\text{CEI}}$ in the boundary condition and $\chi_{\perp,i}/\chi_{\perp,e} = 2$ in the pedestal. $P_{e,\text{in,edge}}^{\text{sim}} = 75$ kW, $P_{i,\text{in,edge}}^{\text{sim}} = 135$ kW, about 64% of total input power is carried by ions at

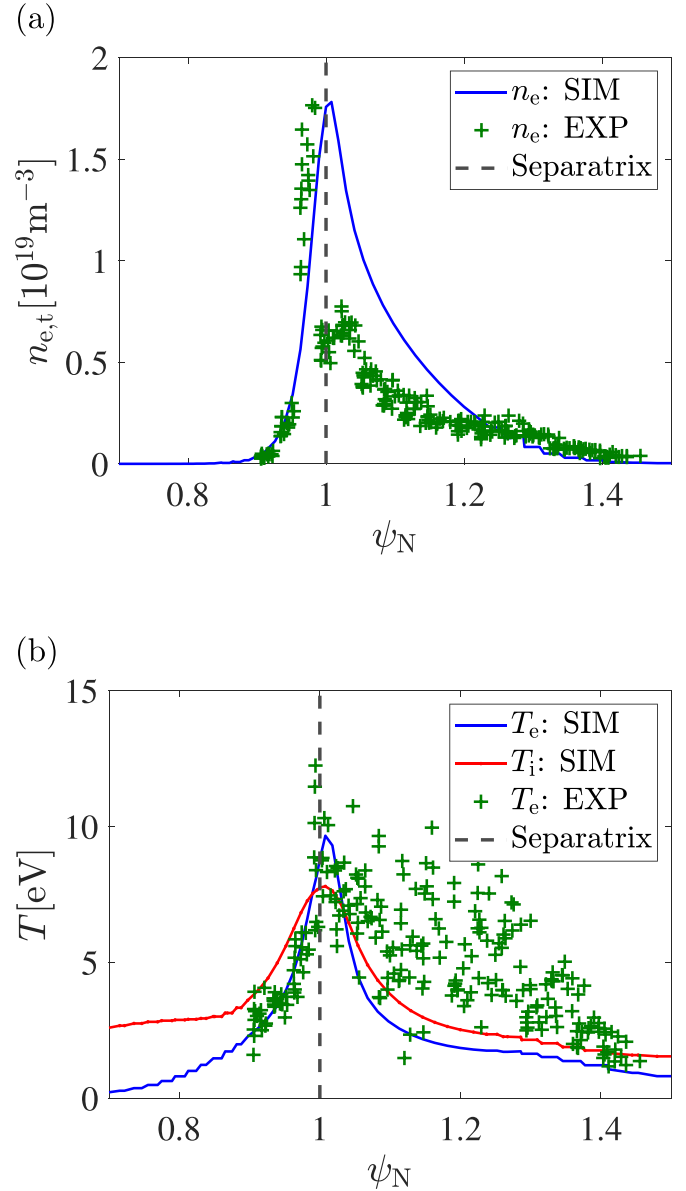


Figure 5. The density and temperature profiles at the outer target, comparing between the experimental measurements (green plus sign, data from *Langmuir Probes* (LP) [58, 59]) and the SOLEDGE-EIRENE simulation (blue and red curves). The dashed line represents the position of separatrix.

the CEI. In the experiment, more heat in the ion channel is due to NBI. The input power $P_{\text{in,edge}}^{\text{sim}}$ found by the simulation code is roughly half of the experimental heating power crossing the CEI: $P_{\text{in,edge}}^{\text{exp}} = P_{\text{in}}^{\text{exp}} - P_{\text{rad,core}}^{\text{exp}} = 430$ kW (table 1). This indicates that, in the experiment, a significant fraction of the injected power is expelled from the core during the ELMs.

The upstream and target profiles, including density, temperature, and carbon concentration demonstrate a good match between experiment and simulations, as shown in figures 3 and 5.

In the experiment, the neutral pressure was measured using Baratron gauges which are connected to the two ports on the wall (near the OMP and at the target, as shown in figure 1)

Table 2. The neutral pressure from simulation values and experimental measurements.

| Position | $P_{\text{neu,port}}^{\text{sim}}$ (mPa) | $P_{\text{neu,gauge}}^{\text{sim}}$ (mPa) | $P_{\text{neu,gauge}}^{\text{exp}}$ (mPa) |
|----------|--|---|---|
| OMP | 11.6 | 0.7 | <10 |
| Target | 364.0 | 36.8 | 34–36 |

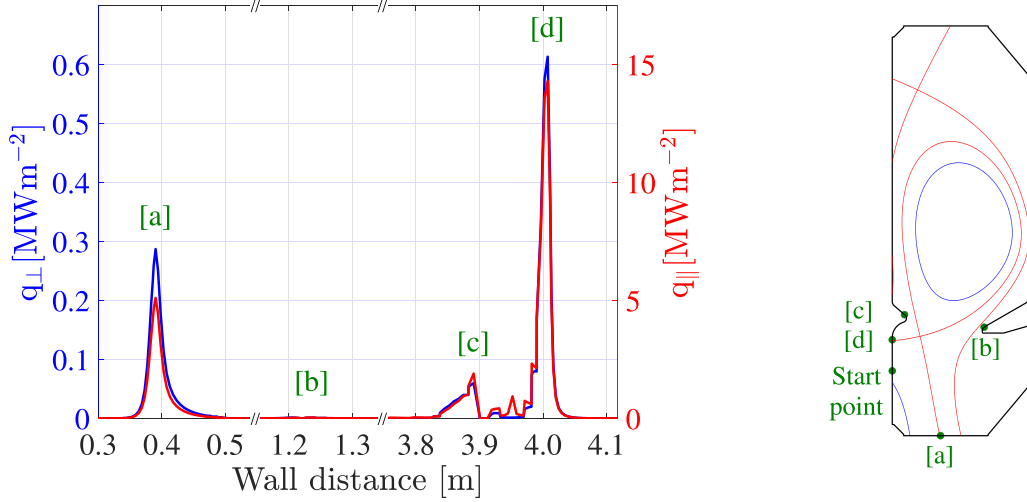


Figure 6. The heat flux on the wall, both perpendicular and parallel, varies as a function of wall distance (integrated counterclockwise along the wall, departs from the start point in PFR, subfigure on the right). The highest heat fluxes are observed near the outer strike point (a), the inner baffle tip (c), and the inner strike point (d). The heat flux between 0.5 m and 3.8 m (including the region near the outer baffle tip (b)) is negligible.

via long tubes to shield the gauges from the magnetic field [60]. The neutral pressure drops quickly in the conducting tube between the Baratron gauge and the port due to the conversion of energetic atomic neutrals to thermal molecules. To relate the measurements from the gauges to the pressure at the port location, we use a 0D-model [15, 61], equations (2) and (3).

$$n_{\text{mol}}^{\text{gauge}} = \frac{n_{\text{atom}}^0}{\sqrt{2}} \sqrt{\frac{T_{\text{atom}}^0}{T_{\text{wall}}}} + n_{\text{mol}}^0 \sqrt{\frac{T_{\text{mol}}^0}{T_{\text{wall}}}} \quad (2)$$

$$p_{\text{gauge}} = n_{\text{mol}}^{\text{gauge}} T_{\text{wall}}, \quad (3)$$

where $n_{\text{mol}}^{\text{gauge}}$ is the molecule density at the gauge. n_{atom}^0 and T_{atom}^0 are the neutral atom density and temperature at the port. n_{mol}^0 and T_{mol}^0 are the neutral molecule density and temperature at the port, respectively. T_{wall} is the temperature of the Baratron tube.

Table 2 shows the value of the averaged neutral pressure obtained from simulations at the port $P_{\text{neu,port}}^{\text{sim}}$, value of neutral pressure at the gauge $P_{\text{neu,gauge}}^{\text{sim}}$ (obtained after the application of the 0D-model, assuming $T_{\text{wall}} = 300$ K in the Baratron tube), and experimental neutral pressure measurements at the gauge $P_{\text{neu,gauge}}^{\text{exp}}$. The $P_{\text{neu,gauge}}^{\text{exp}}$ at the target is in the range of 34–36 mPa (the data at $t = 1.07$ – 1.1 s, considering a relatively slow response time of the entire Baratron system from 70 to 100 ms [60]). The $P_{\text{neu,gauge}}^{\text{exp}}$ near the OMP is below the noise level and difficult to measure. This is compatible with the very

low pressure (0.7 mPa) that the simulation indicates. Overall, the agreement between the experiment and simulation is good.

The heat flux on the wall (figure 6) from the simulation shows that the target heat flux peaks near the inner and outer strike points and at the inner baffle tip, while it was negligible at other positions. In addition, the imbalance between inner and outer targets is noticeable, with the inner target experiencing a higher peak parallel heat flux by a factor of 2–3.

3. Upstream separatrix density scan

The initial simulation setups showed good agreement between the simulations and the measurements. We now investigate the role of the OMP separatrix density on the divertor state. We scan the separatrix density from $n_{\text{e,sep}} = 1.0 \times 10^{19} \text{ m}^{-3}$ to $3.0 \times 10^{19} \text{ m}^{-3}$, while employing a feedback-controlled deuterium gas puff rate in the simulations. The input power ($P_{\text{e,in,edge}}^{\text{sim}} = 75$ kW, $P_{\text{i,in,edge}}^{\text{sim}} = 135$ kW), diffusion coefficients, and other setups were kept unchanged.

3.1. Evolution of multiple parameters

Figure 7 shows the evolution of multiple parameters. Here, T_{sep} is the upstream separatrix temperature. $\langle n_{\text{C,total}} \rangle_{\text{div}}$ is the divertor-averaged total carbon density (sum of all charge states: $\text{C}^0 \rightarrow \text{C}^{6+}$, averaged along the lower part of outer divertor leg, blue line in figure 1). $\hat{T}_{\text{e,t}}$, $\hat{n}_{\text{e,t}}$, $\hat{\Gamma}_{\parallel,\text{i,t}}$ and $\hat{q}_{\parallel,\text{t}}$ are the

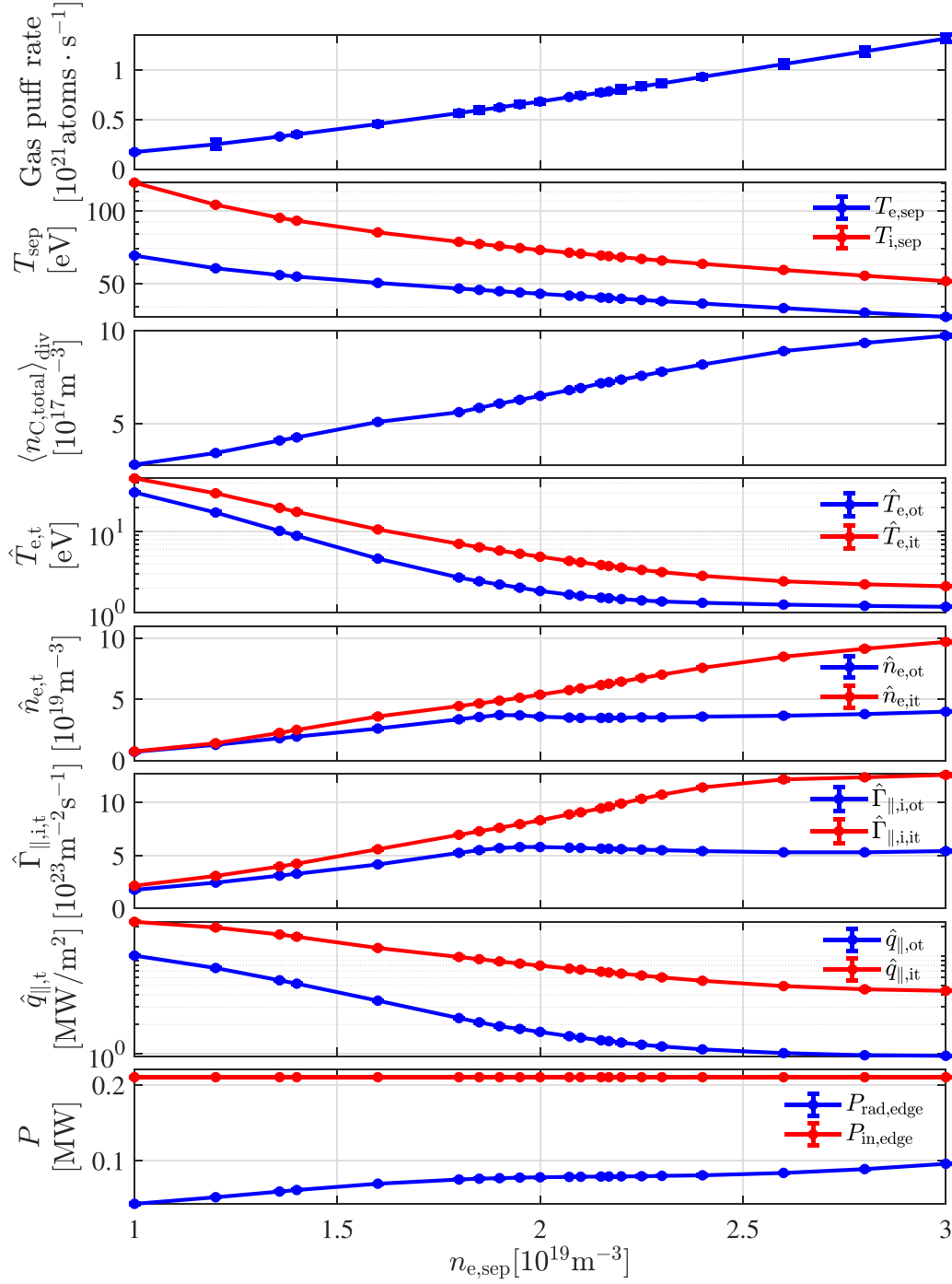


Figure 7. Evolution of several simulated fields as a function of $n_{e,sep}$ in steady-state simulations.

peak electron temperature, density, parallel ion flux, and parallel heat flux at the targets respectively. $P_{rad,edge}^{sim}$ is the total radiated power in the simulation domain. $P_{in,edge}^{sim}$ is the total input power entering the simulation domain. We use the subscript ‘it’ and ‘ot’ to indicate the inner and outer targets, respectively. As $n_{e,sep}$ increases, we can observe that:

- The amount of deuterium that needs to be supplied through gas puff increases approximately linearly with the $n_{e,sep}$.
- The upstream separatrix electron and ion temperatures, $T_{e,sep}$ and $T_{i,sep}$, decrease. The difference in ion and electron temperatures at the separatrix reduces due to the increased collisionality.
- The divertor-averaged total carbon density $\langle n_{C,total} \rangle_{div}$ increases due to a higher level of carbon sputtered from the graphite wall tiles.
- The peak particle flux rolls over only at the outer target in the range of $n_{e,sep}$ investigated. With a peak target temperature lower than 2 eV at the outer target, a 90% decrease

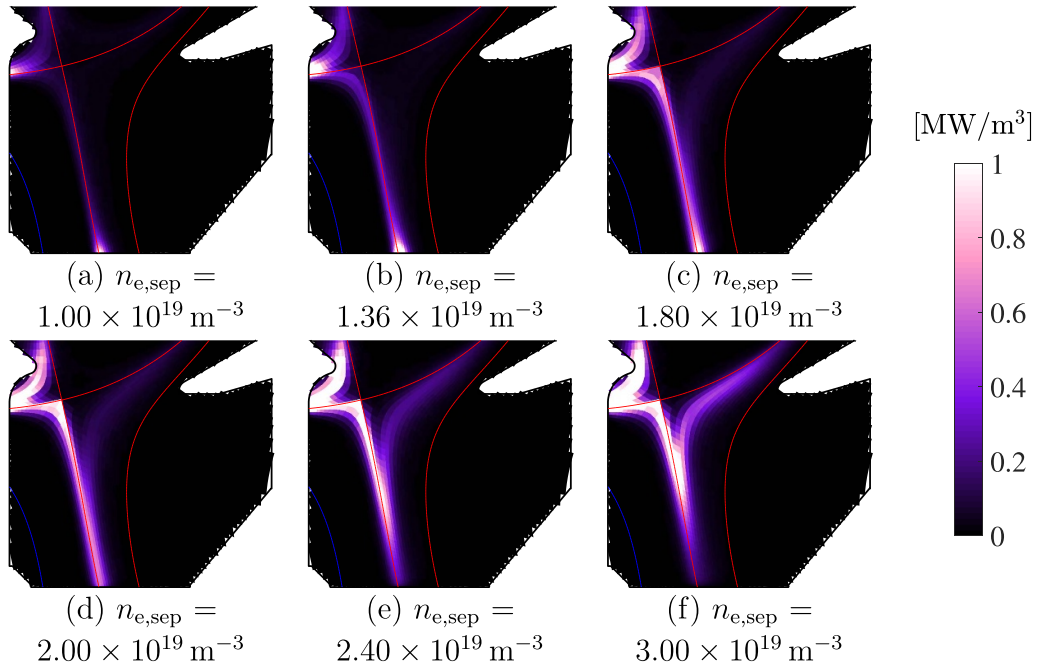


Figure 8. Simulated 2D maps of P_{rad} , from (a) to (f) with increasing $n_{e,\text{sep}}$. In order to highlight the radiation front region, the upper limit of color bar is set as 1 MW m^{-3} , even if the peak value of radiation can be 10 MW m^{-3} , occur at the inner target, in some cases.

in the deposited heat flux, and momentum loss $f_{\text{mom,loss}} = 1 - P_{\text{total,target}}/P_{\text{total,upstream}} > 0.85$, the outer divertor has reached the detached regime. To investigate the properties of detachment, the following analyses will mainly focus on the outer divertor leg. The rollover of particle flux integrated over the outer target is typically observed (along with peak particle flux rollover) to identify detachment in TCV experiments, while in the simulations, it does not exhibit a rollover within the range of $n_{e,\text{sep}}$ studied. This may be due to the absence of the MAR in the simulations, which were shown in [40] to play a significant role in TCV.

- Higher fraction of the power is radiated with a fixed input power $P_{\text{in,edge}}^{\text{sim}}$.

3.2. Evolution of radiation front

Energy losses in the plasma before reaching the targets can occur either due to plasma interaction with neutrals or impurity radiation. Hence, it is crucial to examine the changes in the total radiated power. As shown in figure 8, with increasing $n_{e,\text{sep}}$, the total radiated power increases gradually. Initially, most of the radiation is concentrated near the strike point regions at the target. As $n_{e,\text{sep}}$ further increases, the radiation tends to increase along the separatrix from the strike-points to the X-point, and in the region near the inner baffle. However, beyond a certain threshold ($n_{e,\text{sep}} \approx 1.8 \times 10^{19} \text{ m}^{-3}$), the radiation at the outer strike point starts to decrease, and the peak radiation region moves up along the separatrix, detaching from the outer target. In the outer divertor area (cyan polygon in figure 9), the power radiated by carbon remains approximately constant (16–19 kW), across the density scan with constant

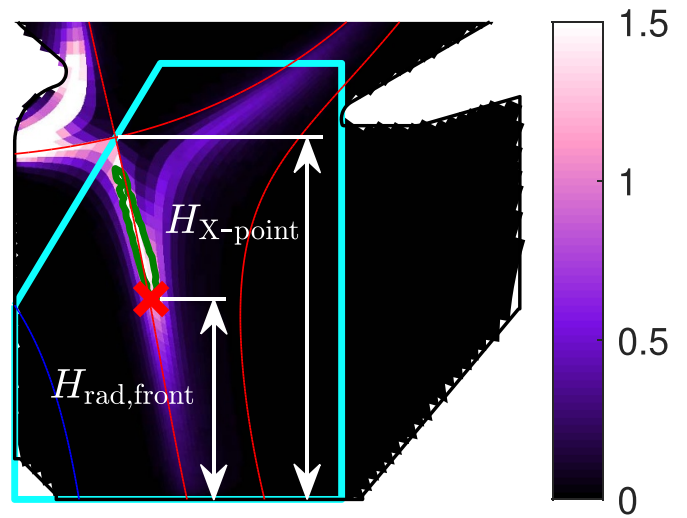


Figure 9. Simulated 2D map of P_{rad} (MW m^{-3}), the same case as (f) in figure 8. For the outer divertor, the radiation front (marked by red cross) is defined as the lowermost point of a region (enclosed by green curve) inside which the P_{rad} of each point is higher than 70% of maximum radiation in the analyzed spatial domain (marked by cyan polygon). The height of the radiation front $H_{\text{rad,front}}$ and the height of X-point $H_{\text{X-point}}$ are defined as the vertical distance between the outer target and the radiation front or X-point, respectively.

SOL input power, with CIII accounting for the majority of the radiation ($\approx 41\%$).

To evaluate the movement of the peak radiation region, there are two commonly employed options: identifying the radiation center, which corresponds to the position that shows the maximum radiation, or the radiation front, which encloses

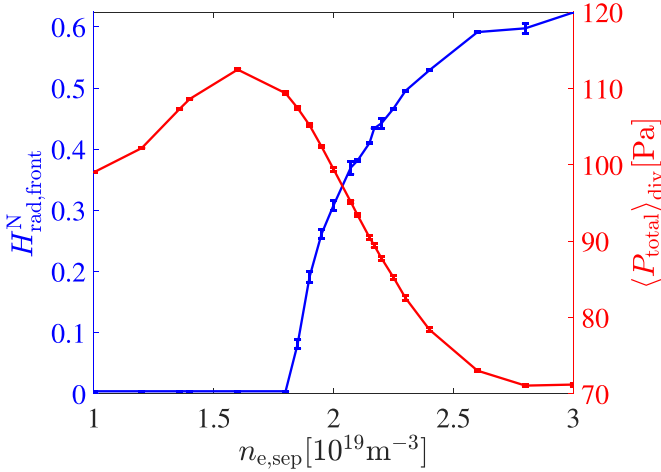


Figure 10. Evolution of normalized radiation front height and total plasma pressure averaged along the lower part of outer divertor leg (blue line in figure 1) as a function of $n_{e,sep}$, in the simulation.

an area that covers most of the radiation. Since the location of maximum radiation will shift closer to the X-point shortly after achieving divertor detachment, identifying the radiation front becomes a more feasible option. As shown in figure 9, we define the radiation front (marked by red cross) as the lowermost point of a region (enclosed by green curve) inside which the P_{rad} of each point is higher than 70% of maximum radiation in the analyzed spatial domain (marked by cyan polygon). The radiation front height $H_{rad,front}$ is used to describe the distance between the radiation front and the target. It is here defined as the vertical distance between the front and the outer target. For comparison between different devices and magnetic configurations, a normalized radiation front height $H_{rad,front}^N$ is the preferred choice, which is defined as the ratio between radiation front height $H_{rad,front}$ and X-point height $H_{X-point}$. In the case of an approximately horizontal divertor leg, the heights are replaced by the distances from the target along the leg. Therefore, $H_{rad,front}^N = 1$ corresponds to the radiation front reaching the X-point height.

We now evaluate the evolution of the radiation front with increasing upstream density. Figure 10 shows that the normalized radiation front height increases with $n_{e,sep}$ once its value exceeds a threshold ($n_{e,sep} \approx 1.80 \times 10^{19} \text{ m}^{-3}$). This threshold is lower than the rollover threshold of particle flux ($n_{e,sep} \approx 1.95 \times 10^{19} \text{ m}^{-3}$, as shown in figure 7). The upward movement of the radiation front also correlates with the total pressure drop along the divertor leg, indicating that the radiation front detachment can serve as an indicator for divertor detachment.

4. Impact of divertor closure

We now investigate the impact of divertor closure in the TCV H-mode case by changing the length of the outer baffle, from the *short inner long outer* geometry to the *short inner short outer* geometry [62], as shown in figure 1. Except for the wall

geometry, the shorter baffle cases keep all parameters identical to the long baffle case described in section 2.

The simulations predict that the longer baffle case exhibits a higher divertor neutral pressure, particularly in the middle part of the outer divertor leg (figure 11), for a given upstream density. This corresponds to a higher effectiveness in trapping neutral particles in the divertor, leading to a higher momentum dissipation level. The difference in neutral pressure distribution due to the change in baffle length can thus influence the detachment onset: the long baffle case demonstrates a lower detachment threshold in $n_{e,sep}$ by up to 16% with respect to the short baffle case. This is consistent with the studies of divertor closure in TCV [14–18], and in other tokamak devices as mentioned in the introduction.

High divertor neutral pressure is required for high-performance operation in ITER [63]. It is interesting to note that, despite the difference in divertor closure, a consistent detachment threshold is found in the simulation cases when considering the divertor neutral pressure (averaged along the lower part of the outer divertor leg, blue line in figure 1). This is illustrated in figure 12 where the detachment threshold is ≈ 0.76 Pa. This finding suggests that the divertor neutral pressure can be used as an ordering parameter for the divertor state when applying constant SOL input power, independently of the divertor configuration.

5. Impact of nitrogen seeding

Using the long and short baffle TCV cases with D and C, nitrogen seeding is introduced to investigate how it will influence the divertor state. As shown in table 3, in addition to the previously studied simulations, three sets of simulations are added: two with *ramped Nitrogen Seeding starting From an Attached case* (NSFA) with long and short baffle, and one with *ramped Nitrogen Seeding starting From a Detached case* (NSFD) with long baffle. When ramped nitrogen seeding is applied, the deuterium puff rate remains unchanged. The two NSFA simulations with long and short baffles have a similar upstream density ($n_{e,sep} \approx 1.35 \times 10^{19} \text{ m}^{-3}$) at the start of seeding. The long baffle NSFD simulation has higher upstream density ($n_{e,sep} \approx 2.07 \times 10^{19} \text{ m}^{-3}$) at the start of seeding. The ramped-up nitrogen seeding or deuterium puff rate leads to an increase in nitrogen concentration, a decrease in carbon concentration in the divertor, and a decrease in the peak electron temperature at the outer target, as shown in figure 13. We define impurity concentration $c_Z = \langle P_{neu,Z} \rangle_{div} / \langle P_{neu,total} \rangle_{div}$ (the ratio of neutral pressure between impurity species and total one, averaged along the lower part of outer divertor leg, blue line in figure 1).

5.1. Simulations with unchanged divertor closure

This section primarily focuses on the impact of nitrogen seeding on the divertor state. Three sets of long baffle simulations (one set without nitrogen seeding and two sets with nitrogen seeding) are compared. Figure 14(a) shows the evolution of $n_{e,sep}$ as a function of peak electron temperature at the outer

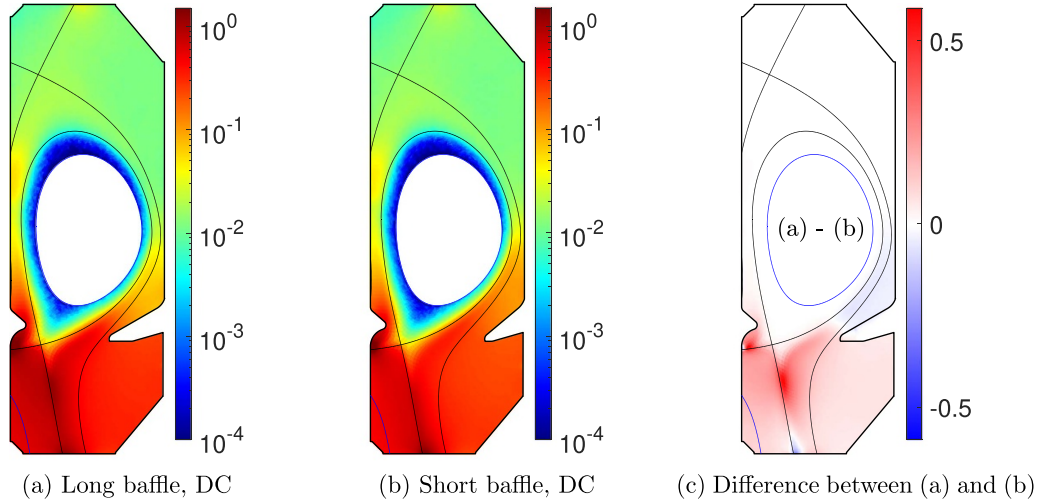


Figure 11. 2D maps of P_{neu} [Pa] are shown in (a) and (b), which have the same upstream separatrix density ($n_{e,\text{sep}} = 3.00 \times 10^{19} \text{ m}^{-3}$) but different baffle lengths. Plot (c) shows the change in neutral pressure [Pa] between (a) and (b) when the baffle length is increased while keeping $n_{e,\text{sep}}$ constant.

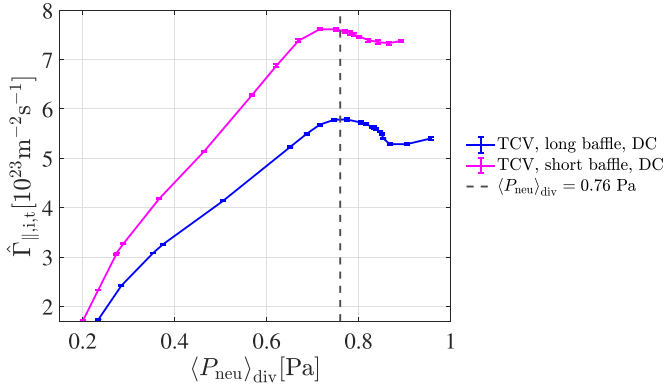


Figure 12. Evolution of peak particle flux at the outer target as a function of divertor-averaged neutral pressure in TCV with different divertor closure levels. The ‘DC’ in the legend indicates the species (deuterium and carbon) present in the simulation.

Table 3. The deuterium and nitrogen puff rate applied in the simulation cases.

| Cases | D_2 puff rate [$10^{21} \text{ atoms} \cdot \text{s}^{-1}$] | N_2 seeding rate [$10^{21} \text{ atoms} \cdot \text{s}^{-1}$] |
|-------------------------|--|---|
| Long baffle, DC | 0.17 → 1.31 | 0 |
| Long baffle, DCN, NSFD | 0.72 | 0 → 0.8 |
| Long baffle, DCN, NSFA | 0.33 | 0 → 1.0 |
| Short baffle, DC | 0.13 → 0.90 | 0 |
| Short baffle, DCN, NSFA | 0.24 | 0 → 1.1 |

target. It is evident that the simulation without nitrogen seeding requires a relatively high $n_{e,\text{sep}}$ to achieve a low target temperature. However, the simulation with nitrogen seeding starting from an attached state can achieve a similar target temperature with a lower $n_{e,\text{sep}}$, which remains relatively constant throughout the scan. This suggests that nitrogen seeding can cool the target temperature with little effect on the upstream density.

The divertor neutral pressure is strongly related to the upstream density in the simulation without nitrogen seeding, figure 14. However, when nitrogen seeding is introduced starting from the attached case, the divertor neutral pressure remains constantly lower, following a behavior similar to that of $n_{e,\text{sep}}$. This observation is consistent with the experimental results [7], indicating that the divertor neutral pressure is strongly related to the upstream electron density and insensitive to nitrogen injection. However, when nitrogen seeding is introduced starting from a detached case, the divertor neutral pressure drops rapidly. Cases (ii) and (iii) in figure 14(b) have similar upstream density ($n_{e,\text{sep}}^{\text{ii}} \approx 2.4 \times 10^{19} \text{ m}^{-3}$ compared to $n_{e,\text{sep}}^{\text{iii}} \approx 2.2 \times 10^{19} \text{ m}^{-3}$) but present a significant difference in divertor neutral pressure (0.85 Pa compared to 0.57 Pa) due to nitrogen injection. Further studies show that introducing nitrogen seeding starting from the detached case rapidly decreases the target particle flux, as shown by the red curve in figure 15(a). Fewer neutral particles are recycled from the target, as a result, divertor neutral pressure decreases. Next, we use the *Two-Point Model* (2PM) to explain how the target particle flux is influenced by nitrogen. As the upstream heat flux $q_{\parallel,u}$ remains relatively constant throughout the scan in the simulations, equation (17) in [64] can be simplified to:

$$\Gamma_{\parallel,e,t}^{\text{2PM}} \propto P_{\text{total},u}^2 \frac{(1 - f_{\text{mom,loss}})^2}{(1 - f_{\text{cooling}})}, \quad (4)$$

where the P_{total} represents the total plasma pressure, the $f_{\text{mom,loss}}$ and f_{cooling} represent the momentum loss fraction and power loss fraction. The subscripts ‘u’ and ‘t’ in the parameters indicate upstream and target, respectively. As shown in figure 15(b), the nitrogen seeding leads to a drop in the upstream pressure ($P_{\text{total},u}$) with little effects on the loss of momentum from upstream to the target ($P_{\text{total},u} - P_{\text{total},t}$). While both the upstream pressure and the loss of momentum increase with $n_{e,\text{sep}}$ by applying a ramped-up deuterium puff rate. In figure 15(c), the $(1 - f_{\text{mom,loss}})^2 / (1 - f_{\text{cooling}})$ evolves

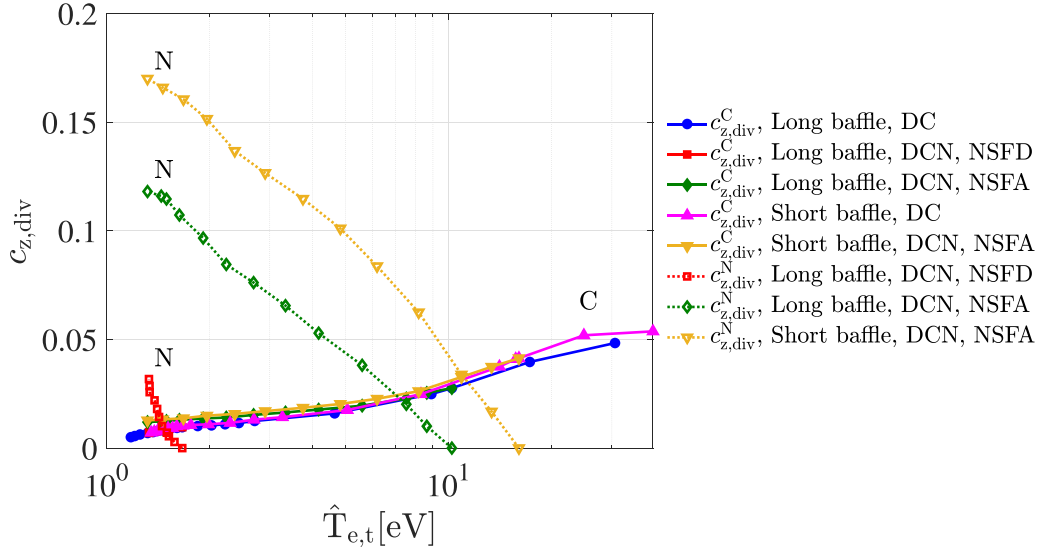


Figure 13. Evolution of carbon and nitrogen concentration ($c_{z,div}^C$ and $c_{z,div}^N$, respectively) as a function of peak electron temperature $\hat{T}_{e,t}$ at the outer target.

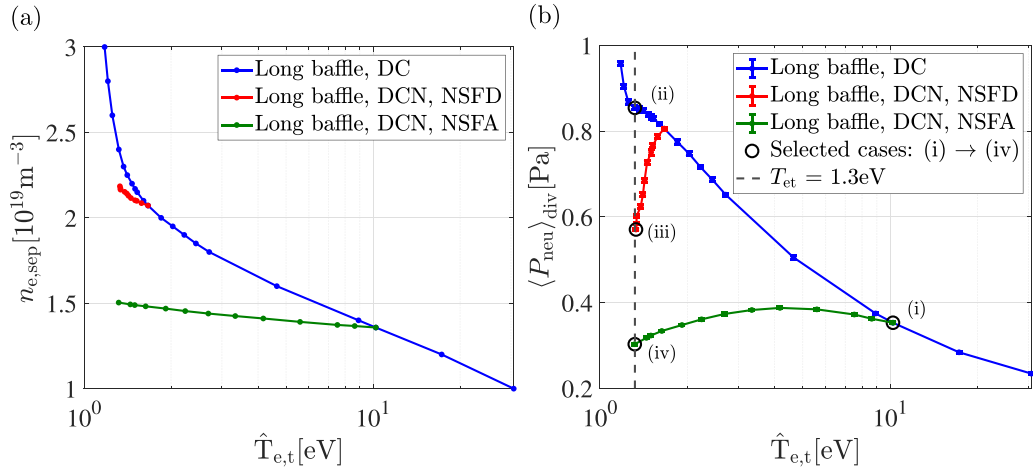


Figure 14. (a) Evolution of upstream separatrix density $n_{e,sep}$ as a function of peak electron temperature at the outer target. (b) Evolution of divertor-averaged neutral pressure (the position of $P_{neu,div}$ is shown in figure 1) as a function of peak electron temperature at the outer target. There are four cases selected: (i) represents an attached case without nitrogen seeding and with a peak target temperature $T_{e,t} = 9.6$ eV. (ii) \rightarrow (iv), represent the detached cases with increasing nitrogen concentration (from 0 to 0.12) and with approximately the same peak target temperatures $T_{e,t} = 1.3$ eV.

with approximately the same slope, particularly the red curve is matched with the blue curve, despite the difference in nitrogen seeding. The $f_{mom,loss}$ and $f_{cooling}$ of the red curve are slightly higher than that of the blue curve for the same peak electron temperature at the outer target. Therefore, the rapid decrease in the target particle flux and drops in the divertor neutral pressure, observed when introducing nitrogen seeding starting from a detached case, are due to the collapse of upstream pressure caused by the nitrogen seeding. This seeding effectively limits the increase of $n_{e,sep}$, while simultaneously reducing the upstream temperature at the same rate as the case without nitrogen seeding. As a result, the upstream pressure drops.

The 2D maps in figure 16 show the distribution of electron temperature, total plasma pressure, and neutral pressure for each of the cases highlighted in figure 14(b). Case (ii) achieves detachment by increasing gas fuelling, consequently elevating the divertor neutral pressure compared to case (i). However, as nitrogen concentration increases in cases (iii) and (iv), the required divertor neutral pressure gradually decreases. This phenomenon can be explained by considering the power balance, since nitrogen is significantly more effective at cooling the divertor compared to deuterium neutrals. For example, when comparing cases (ii) and (iv), assuming the influence of carbon is negligible, the efficiency of nitrogen compared to deuterium, denoted as f_z^N [65], results in the overall influence

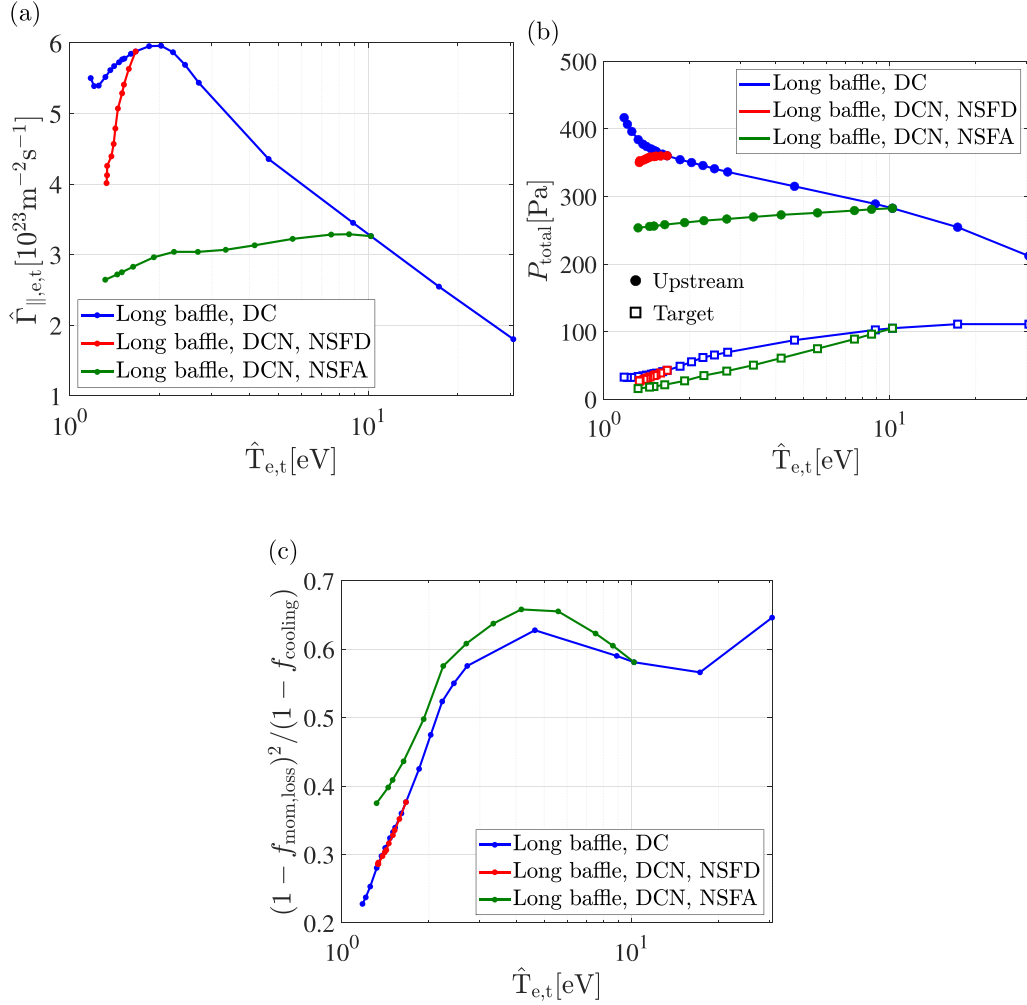


Figure 15. (a) Evolution of peak parallel electron particle flux as a function of peak electron temperature at the outer target. (b) Evolution of total plasma pressure at the upstream and outer target. (c) Evolution of $(1 - f_{\text{mom,loss}})^2 / (1 - f_{\text{cooling}})$, where $f_{\text{mom,loss}}$ and f_{cooling} represent momentum loss fraction and power loss fraction, respectively.

of neutral particles (nitrogen and deuterium) in case (iv) being approximately equal to the influence of only deuterium in case (ii) in the divertor, in terms of achieving the same peak target temperature $\hat{T}_{e,t} = 1.3$ eV, as expressed by the following equation:

$$f_z^N \cdot \langle P_{\text{neu},N} \rangle_{\text{div}}^{(\text{iv})} + \langle P_{\text{neu},D} \rangle_{\text{div}}^{(\text{iv})} = \langle P_{\text{neu},D} \rangle_{\text{div}}^{(\text{ii})}, \quad (5)$$

where $\langle P_{\text{neu},N} \rangle_{\text{div}}^{(\text{iv})}$ represents the divertor nitrogen neutral pressure of case (iv), $\langle P_{\text{neu},D} \rangle_{\text{div}}^{(\text{iv})}$ and $\langle P_{\text{neu},D} \rangle_{\text{div}}^{(\text{ii})}$ represent the divertor deuterium neutral pressure of case (iv) and case (ii), respectively. Therefore, we obtain $f_z^N \approx 16.4$, close to the $f_z^N = 18$ used in the partial detachment model in [65], which will later be compared with the simulations in section 6.

Figure 17 shows the evolution of radiated power from different species in simulations with and without nitrogen seeding. As the deuterium or nitrogen gas puff rate increases, the peak target temperature $\hat{T}_{e,t}$ decreases in both simulations (from 10 eV to 1.5 eV). The radiated power from carbon remains approximately constant (≈ 48 kW) in the $n_{e,\text{sep}}$

ramp-up simulation (figure 17(a)) and is reduced (from 44 kW to 28 kW) in the nitrogen ramp-up simulation (figure 17(b)) as a function of decreasing target temperature. The limited role of carbon in achieving detachment is evident since there is little change in power dissipation by carbon with reduced temperature.

In the simulation without nitrogen seeding (only D and C), despite more than 50% of power being radiated by carbon (figure 17(a)), the increased power dissipation with increasing upstream density is mainly due to deuterium emission, driven by the neutral pressure level in the divertor.

When nitrogen is seeded starting from the attached case (as shown in figure 17(b)), it eventually replaces carbon and deuterium as the dominant radiation source, accounting for more than 65% of radiated power for $\hat{T}_{e,t} < 2$ eV, with a nitrogen concentration lower than 0.12 in the divertor, figure 13. This is consistent with previous simulation observations [38, 53]. The radiated power from deuterium remains constant with decreasing $\hat{T}_{e,t}$ due to constantly lower divertor neutral pressure.

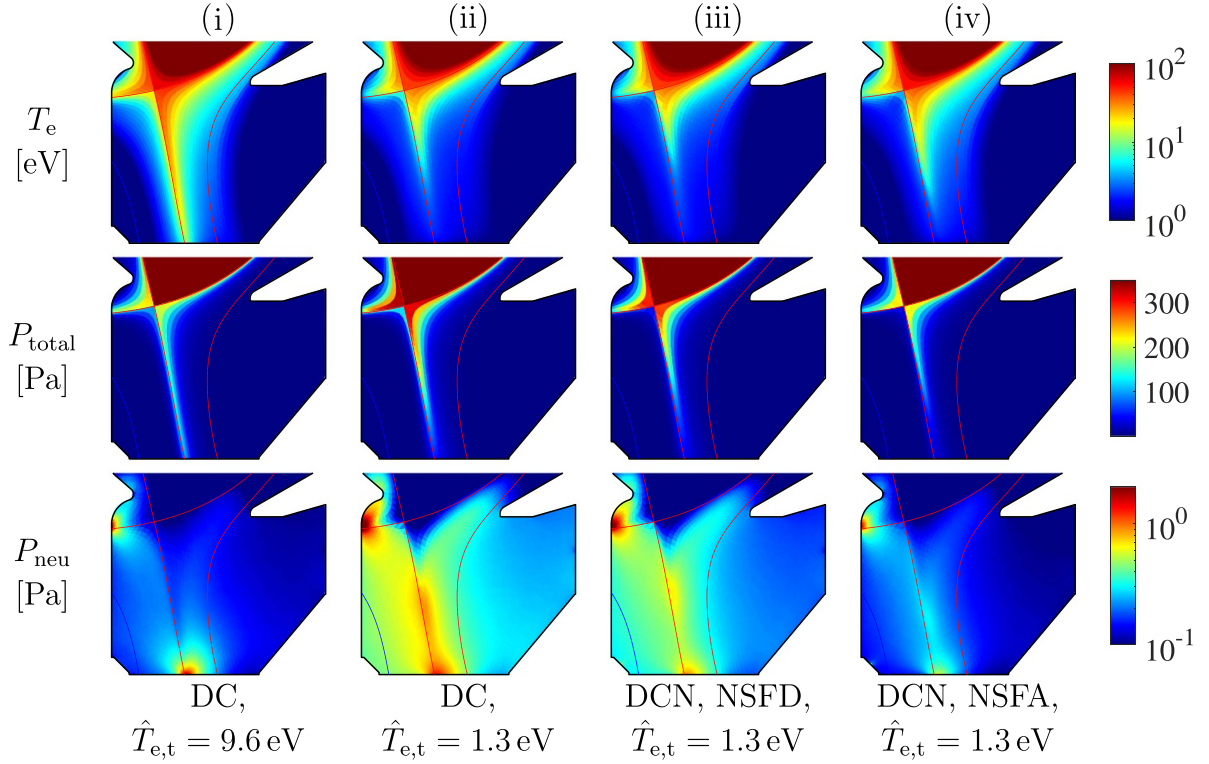


Figure 16. 2D maps of variables for selected cases (i)–(iv) marked in figure 14(b): electron temperature T_e in the first row, total plasma pressure P_{total} in the second row, and neutral pressure P_{neu} in the third row.

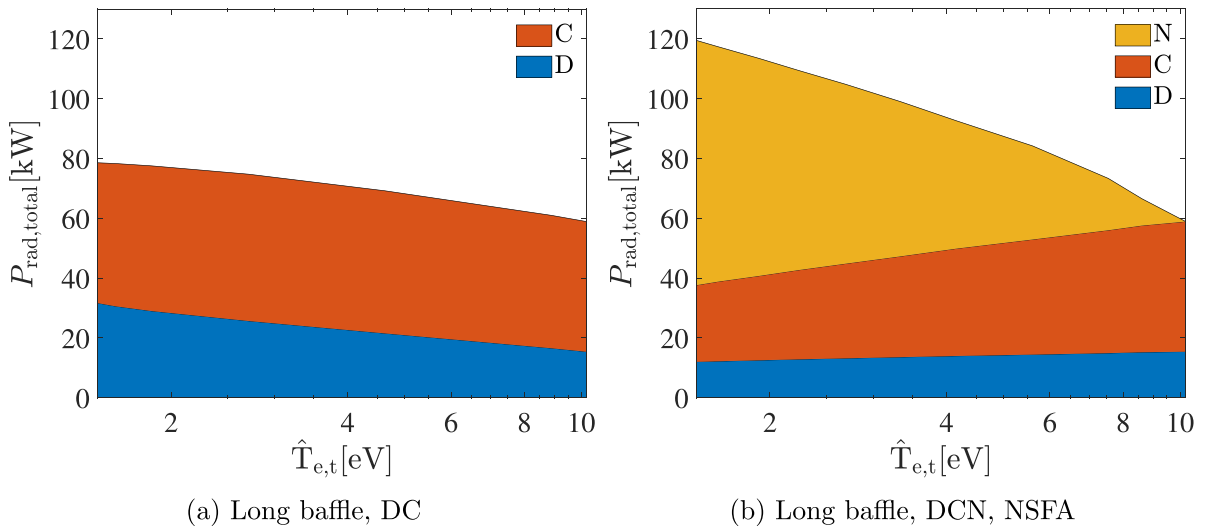


Figure 17. (a) Evolution of radiation from different species as a function of peak electron temperature at the outer target in DC simulation. (b) Evolution of radiation from different species in DCN simulation with nitrogen seeding starting from attached.

Nitrogen plays an important role in radiative power dissipation, and it is found localized in the region of low temperature close to the target [53]. Reaching detachment with nitrogen seeding and pure deuterium puff leads to different radiation profiles along the divertor outer leg for the same target heat flux. In particular, with nitrogen seeding, the emission front appears closer to the target, as shown in figure 18.

5.2. Simulations with changed divertor closure

In section 4, we discussed that the change in baffle length can influence the neutral pressure distribution (mainly deuterium) so that the long baffle simulation has a lower detachment threshold in terms of upstream density $n_{e,\text{sep}}$. In this section, we study if the effect of nitrogen is influenced by

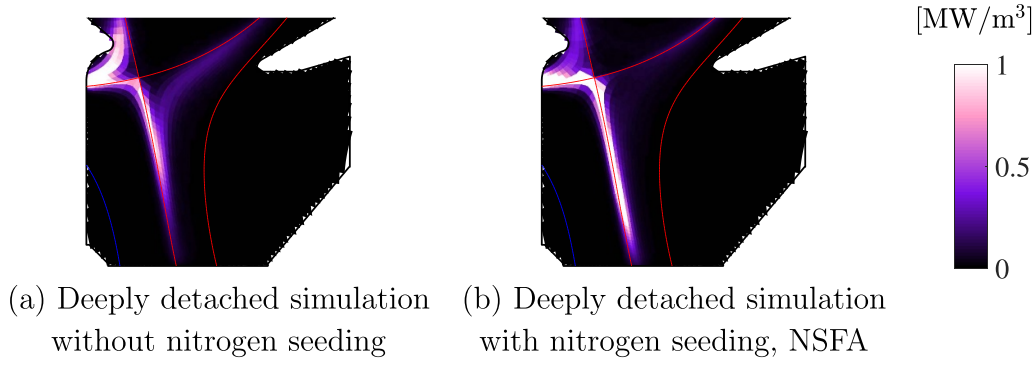


Figure 18. 2D plots of P_{rad} for two long baffle cases with similar $\hat{q}_{\parallel, \text{ot}}$ about 1.12 MW m^{-2} .

divertor closure. When discussing the impact of nitrogen seeding on detachment, it is more practical to consider the point at which the radiation front starts moving upwards from the target ($H_{\text{rad, front}}^N \geq 0.05$) as a sign of divertor detachment, particularly for identifying the threshold of detachment. This is because the ramped nitrogen seeding rate leads to a direct decrease in the target ion flux, similar to the target electron flux in figure 15(a), making it difficult to identify the rollover threshold. Experimental nitrogen seeding discharges also show a significant decrease in particle flux with respect to the discharge without nitrogen [7, 8, 66].

In figure 19(a), we observe that for the ramped nitrogen seeding simulations starting from attached, the radiation front detachment threshold in $n_{e, \text{sep}}$ is almost unchanged between the two baffle lengths ($\approx 1.4 \times 10^{19} \text{ m}^{-3}$), thus the influence of neutral pressure is equivalent in both simulations. However, the radiation front detachment threshold in nitrogen concentration is lower by 50% in the long baffle simulation compared with the short baffle simulation. The effects of carbon are neglected due to low carbon concentration ($c_{\text{C, div}} \approx 0.018$ compared to $c_{\text{N, div}} \approx 0.05\text{--}0.1$ when the plasma detaches, carbon is also approximately half as effective as nitrogen in power radiation, discussed in section 6). This observation confirms that increased divertor closure can also facilitate the detachment process with nitrogen seeding as reduced nitrogen concentration is required.

TCV simulations with or without nitrogen seeding show different results in $\hat{T}_{e, t}$ threshold for radiation front detachment as shown in figure 19(b). Two simulations without nitrogen seeding detach at $\hat{T}_{e, t} \approx 2.5 \text{ eV}$, while two simulations with nitrogen seeding (starting from attached) detach at $\hat{T}_{e, t} \approx 5 \text{ eV}$. When a sufficient amount of nitrogen is present, it is possible to radiate enough power to achieve radiation front detachment even at higher divertor temperatures (between 5 and 10 eV). In contrast, if nitrogen seeding is not used, a lower divertor temperature (2.5–5 eV) is required to achieve a similar level of power dissipation. Despite the difference in target temperature threshold influenced by nitrogen, we observe approximately the same heat flux threshold $\approx 2.3 \text{ MW m}^{-2}$ for the radiation front to begin moving upward from the target, as shown in figure 19(c). Furthermore, the lower radiation front in the nitrogen seeding case (figure 18) can also be verified through figure 19(c), where one can observe that the radiation front

height in the high nitrogen concentration simulation is generally lower than the one with lower nitrogen concentration or without nitrogen for a given target heat load in deeply detached divertor.

6. Comparison with partial detachment model

To predict the relation between input power, divertor neutral pressure, and impurity concentration under partially detached conditions (detachment of the first few power widths in the SOL) in arbitrarily sized machines, a simplified model based on an empirical formula has been proposed [65]. This model was calibrated on AUG experimental data and is currently assumed to only be relevant for divertors of similar geometry. The model is shown in equation (6).

$$q_{\text{det}} = \frac{P_{\text{sep}}}{R} \left[p_0 (1 + f_z c_z) \cdot \left(\frac{\lambda_{\text{int}}}{0.005} \right) \cdot \left(\frac{R}{1.65} \right)^{r_z} \right]^{-1} \times 1.3 \text{ Pa m MW}^{-1}, \quad (6)$$

where $q_{\text{det}} = 1$ corresponds to the partial detachment state. We now explain the terms in equation (6) and try to apply this model to the TCV simulation data.

- P_{sep} represents the input power across the separatrix.
- $R = 0.88 \text{ m}$, the major radius.
- p_0 the average total neutral pressure under the baffle ($P_{\text{neu, baffle}}$ in figure 1).
- f_z the relative efficiency of impurity to achieve detachment compared to deuterium. For nitrogen $f_z^N = 18$ [65], f_z^C is estimated to be 10 since higher concentration (by a factor 1.83) is required to obtain the same upstream power for given target parameters, when replacing N by C [67]. The influence of f_z^C value is quite small since the carbon concentration is low (less than 5%).
- $f_z c_z$ in this article is calculated as $f_z c_z = f_z^C c_z^C + f_z^N c_z^N$.
- $\lambda_{\text{int}} = \lambda_q + 1.64S$, represents the integral power decay length [68] inside which the divertor power spreading factor S is about $\lambda_q/2$ based on the experimental data in [69]. Checking in the simulation, the ratio λ_q/S increases with increasing upstream density from 1 at low densities to approximately 2 in detached states. λ_q is evaluated based on the target heat flux profile remapped at the OMP.

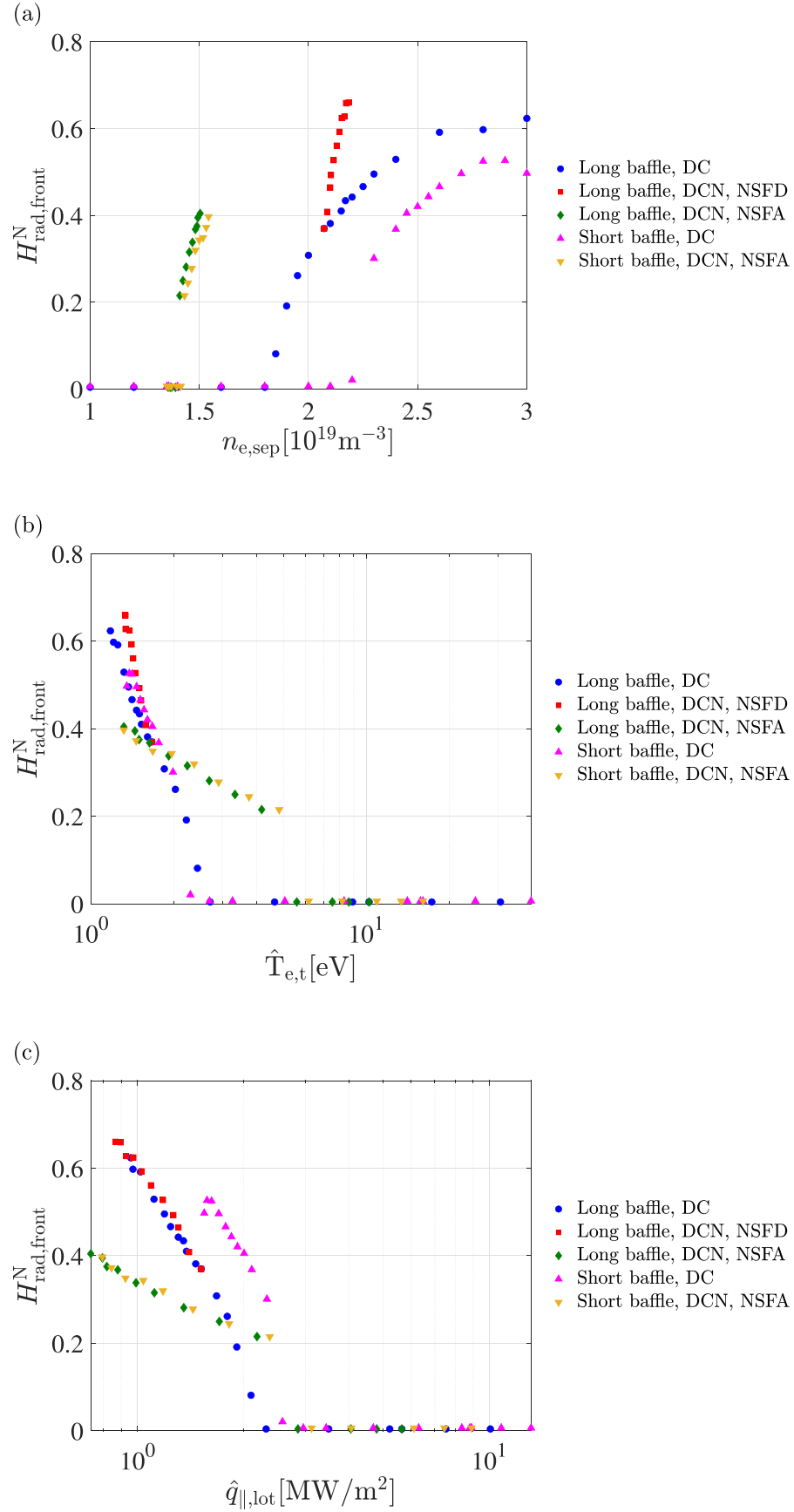


Figure 19. (a) Evolution of normalized radiation front height as a function of $n_{\text{e,sep}}$, (b) as a function of peak electron temperature at the outer target, and (c) as a function of peak parallel heat flux at the outer target.

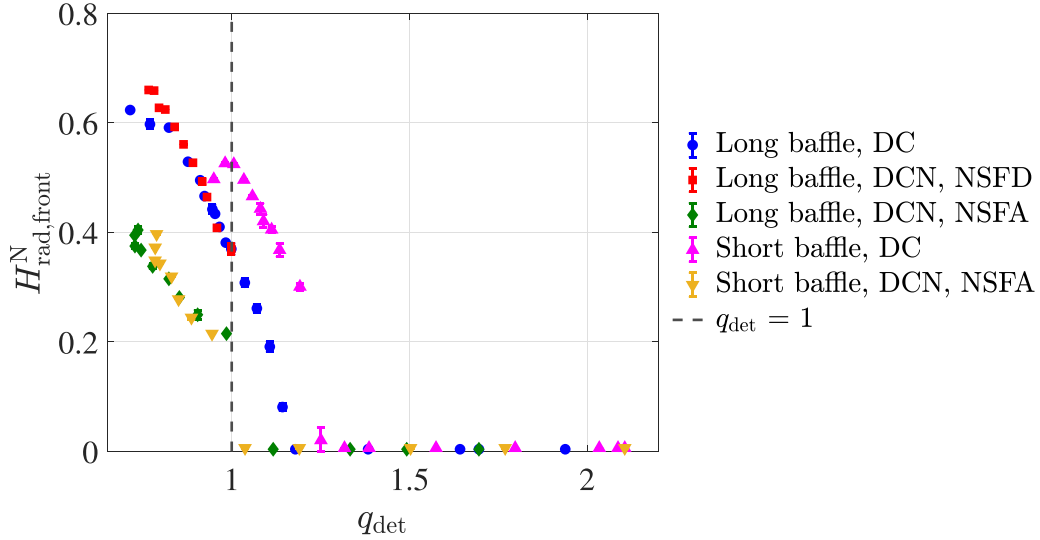


Figure 20. Evolution of normalized radiation front height as a function of q_{det} .

- $r_z = 0.1$ is a weak exponent assuming that the distance where the λ step occurs scales with the major radius.

The evolution of the normalized radiation front height as a function of q_{det} is shown in figure 20. The green and yellow symbols correspond to the long and short baffle simulations with nitrogen seeding starting from the attached, indicating the onset of detachment when $q_{\text{det}} \approx 1$. The model correctly predicts the partial detachment when the simulation has a high level of divertor radiation due to nitrogen, while it predicts a different value at which the detachment starts in the simulations without seeded impurities. The red symbols correspond to the simulation with nitrogen seeding cannot be used to verify the agreements between the qualifier and simulation as it starts directly from the detached case with $q_{\text{det}} \leq 1$. The two simulations with nitrogen seeding starting from the attached state have significantly higher total impurity concentration values than other simulations when the plasma detaches (figure 13), indicating that high enough c_z^N in the divertor can effectively radiate most of the power that enters the divertor, despite a reduction in divertor closure.

7. Conclusion

SOLEEDGE3X-EIRENE has been used to simulate TCV H-mode plasmas, with input parameters carefully selected to reproduce experimental conditions. To gain a better understanding of the confinement properties of H-mode edge plasmas, profile feedback control has been developed as an interpretive tool to extract edge transport coefficients from experimental data.

With fixed input power, divertor detachment is achieved either by increasing the separatrix density or by seeding impurities (nitrogen) in the divertor. Increasing $n_{e,\text{sep}}$ increases both the upstream pressure and momentum dissipation, represen-

ted as increased divertor neutral pressure. Nitrogen seeding reduces the target temperature with little effect on the upstream density and momentum loss but drops the upstream pressure, leading to a decrease in the target particle flux and divertor neutral pressure.

Divertor closure mainly affects the neutral pressure distribution in the divertor. As the divertor closure is increased for the same upstream density, we find that higher divertor neutral pressure leads to a higher power dissipation level, which facilitates detachment. In the constant input power simulations without nitrogen seeding, we observe a robust neutral pressure threshold for detachment, despite the difference in divertor closure, emphasizing the strong relationship between neutral pressure and divertor state.

Introducing nitrogen seeding (with concentration ≈ 0.12 in the divertor) can replace deuterium and carbon as the primary radiation source (65% of power). Sufficient power can be dissipated to achieve radiation front detachment at a higher target temperature threshold since nitrogen is a more effective radiator in the higher temperature range of 5–10 eV. When maintaining the same heat load is required in a detached divertor with constant SOL input power, the case with higher nitrogen concentration allows for a lower radiation front height because nitrogen radiation is mainly localized near the target.

A simple detachment qualifier, which evaluates the collective impact of input power entering the divertor, neutral pressure, and the concentration and species of impurity in achieving divertor detachment, has previously been validated for the ASDEX Upgrade geometry and plasma conditions, predicts partial detachment for TCV simulations with high impurity concentration, as expected, when $q_{\text{det}} \approx 1$. Most of the power that enters the divertor can be effectively radiated by nitrogen with a high enough concentration, despite a reduction in divertor closure. Furthermore, this confirms the potential of the model to be applied in devices of different sizes.

Data availability statement

All data that support the findings of this study are included within the article (and any supplementary files).

Acknowledgments

This work has been carried out within the framework of the EUROfusion Consortium, partially funded by the European Union via the Euratom Research and Training Programme (Grant Agreement No. 101052200—EUROfusion). The Swiss contribution to this work has been funded by the Swiss State Secretariat for Education, Research and Innovation (SERI). Views and opinions expressed are however those of the author(s) only and do not necessarily reflect those of the European Union, the European Commission or SERI. Neither the European Union nor the European Commission nor SERI can be held responsible for them. This work benefited from HPC resources from CINECA Marconi-Fusion (Project FUA36_HEAT and FUA36_TSVV6_22).

ORCID iDs

H Yang  <https://orcid.org/0000-0002-4983-1249>
 O Février  <https://orcid.org/0000-0002-9290-7413>
 D Galassi  <https://orcid.org/0000-0003-3388-4538>
 S Gorno  <https://orcid.org/0000-0003-0524-7283>
 S Henderson  <https://orcid.org/0000-0002-8886-1256>
 H Reimerdes  <https://orcid.org/0000-0002-9726-1519>
 C Theiler  <https://orcid.org/0000-0003-3926-1374>
 N Rivals  <https://orcid.org/0000-0002-4467-5857>

References

- [1] Pitts R A *et al* 2017 Physics conclusions in support of ITER W divertor monoblock shaping *Nucl. Mater. Energy* **12** 60–74
- [2] Zohm H *et al* 2013 On the physics guidelines for a tokamak DEMO *Nucl. Fusion* **53** 073019
- [3] Wischmeier M (The ASDEX Upgrade team and JET EFDA contributors) 2015 High density operation for reactor-relevant power exhaust *J. Nucl. Mater.* **463** 22–29
- [4] Matthews G F 1995 Plasma detachment from divertor targets and limiters *J. Nucl. Mater.* **220–222** 104–16
- [5] Leonard A W *et al* 2012 Scaling radiative divertor solutions to high power in DIII-D *Nucl. Fusion* **52** 063015
- [6] Bernert M *et al* 2020 X-point radiation, its control and an ELM suppressed radiating regime at the ASDEX Upgrade tokamak *Nucl. Fusion* **61** 024001
- [7] Février O *et al* 2020 Nitrogen-seeded divertor detachment in TCV L-mode plasmas *Plasma Phys. Control. Fusion* **62** 035017
- [8] Theiler C *et al* 2018 SOL transport and detachment in alternative divertor configurations TCV L- and H-mode plasmas *27th IAEA Fusion Energy Conf. (FEC 2018)* (available at: <http://infoscience.epfl.ch/record/264809>)
- [9] Bernert M *et al* 2017 Power exhaust by SOL and pedestal radiation at ASDEX Upgrade and JET *Nucl. Mater. Energy* **12** 111–8
- [10] Oberkofler M *et al* 2013 First nitrogen-seeding experiments in jet with the iter-like wall *J. Nucl. Mater.* **438** S258–61
- [11] Harrison J R *et al* 2019 Progress toward divertor detachment on TCV within H-mode operating parameters *Plasma Phys. Control. Fusion* **61** 065024
- [12] Hofmann F *et al* 1994 Creation and control of variably shaped plasmas in TCV *Plasma Phys. Control. Fusion* **36** B277
- [13] Reimerdes H *et al* 2022 Overview of the TCV tokamak experimental programme *Nucl. Fusion* **62** 042018
- [14] Fasoli A *et al* 2019 TCV heating and divertor upgrades *Nucl. Fusion* **60** 016019
- [15] Wensing M *et al* 2019 SOLPS-ITER simulations of the TCV divertor upgrade *Plasma Phys. Control. Fusion* **61** 085029
- [16] Galassi D *et al* 2020 Numerical investigation of optimal divertor gas baffle closure on TCV *Plasma Phys. Control. Fusion* **62** 115009
- [17] Février O *et al* 2021 Divertor closure effects on the TCV boundary plasma *Nucl. Mater. Energy* **27** 100977
- [18] Reimerdes H *et al* 2021 Initial TCV operation with a baffled divertor *Nucl. Fusion* **61** 024002
- [19] Casali L *et al* 2018 Modelling the effect of divertor closure on detachment onset in DIII-D with the SOLPS code *Contrib. Plasma Phys.* **58** 27–9
- [20] Guo H Y *et al* 2019 First experimental tests of a new small angle slot divertor on DIII-D *Nucl. Fusion* **59** 086054
- [21] Shafer M W *et al* 2019 Dependence of neutral pressure on detachment in the small angle slot divertor at DIII-D *Nucl. Mater. Energy* **19** 487–92
- [22] Moser A L *et al* 2019 The effect of divertor closure on detachment onset in DIII-D *Nucl. Mater. Energy* **19** 67–71
- [23] Casali L *et al* 2019 The effect of neutrals in the new SAS divertor at DIII-D as modelled by SOLPS *Nucl. Mater. Energy* **19** 537–43
- [24] Casali L *et al* 2020 Neutral leakage, power dissipation and pedestal fueling in open vs closed divertors *Nucl. Fusion* **60** 076011
- [25] Wang H Q *et al* 2023 Study on divertor detachment and pedestal characteristics in the DIII-D upper closed divertor *Nucl. Fusion* **63** 046004
- [26] Neu R *et al* 2003 The ASDEX Upgrade divertor IIb—a closed divertor for strongly shaped plasmas *Nucl. Fusion* **43** 1191–6
- [27] Loarte A *et al* 1998 Plasma detachment in JET Mark I divertor experiments *Nucl. Fusion* **38** 331–71
- [28] JET Team (prepared by R.D Monk) 1999 Recent results from divertor and scrape-off layer studies at JET *Nucl. Fusion* **39** 1751–62
- [29] Horton L D *et al* 1999 Studies in JET divertors of varied geometry. I: non-seeded plasma operation *Nucl. Fusion* **39** 1–17
- [30] Si H *et al* 2019 Modeling the effect of divertor closure on plasma detachment for new divertor design of EAST by SOLPS *Plasma Phys. Control. Fusion* **61** 095007
- [31] Tao Y Q *et al* 2021 Impact of divertor closure on edge plasma behavior in EAST H-mode plasmas *Plasma Phys. Control. Fusion* **63** 065004
- [32] Asakura N *et al* 1999 Heat and particle transport of SOL and divertor plasmas in the W shaped divertor on JT-60U *Nucl. Fusion* **39** 1983–94
- [33] Yang H *et al* 2022 Numerical modeling of the impact of leakage under divertor baffle in WEST *Nucl. Mater. Energy* **33** 101302
- [34] Bufferand H *et al* 2015 Numerical modelling for divertor design of the WEST device with a focus on plasma–wall interactions *Nucl. Fusion* **55** 053025
- [35] Tamain P *et al* 2016 The TOKAM3X code for edge turbulence fluid simulations of tokamak plasmas in versatile magnetic geometries *J. Comput. Phys.* **321** 606–23
- [36] Zhdanov V M 2002 *Transport Processes in Multicomponent Plasma* (CRC Press)

- [37] Bufferand H *et al* 2019 Three-dimensional modelling of edge multi-component plasma taking into account realistic wall geometry *Nucl. Mater. Energy* **18** 82–86
- [38] Smolders A *et al* 2020 Comparison of high density and nitrogen seeded detachment using SOLPS-ITER simulations of the tokamak α configuration variable *Plasma Phys. Control. Fusion* **62** 125006
- [39] Roth J 1999 Chemical erosion of carbon based materials in fusion devices *J. Nucl. Mater.* **266–269** 51–57
- [40] Verhaegh K *et al* 2021 The role of plasma-molecule interactions on power and particle balance during detachment on the TCV tokamak *Nucl. Fusion* **61** 106014
- [41] Myatra O *et al* 2023 Solps-iter predictive simulations of the impact of ion-molecule elastic collisions on strongly detached mast-u super-x divertor conditions *Nucl. Fusion* **63** 076030
- [42] Pereverzew G V *et al* 1991 An Automatic System for Transport Analysis in a Tokamak *Technical Report* IPP 5/42 (Max-Planck-Institut für Plasmaphysik)
- [43] Hawke J *et al* 2017 Improving spatial and spectral resolution of TCV Thomson scattering *J. Instrum.* **12** C12005
- [44] Duval B P *et al* 2008 Spontaneous L-mode plasma rotation scaling in the TCV tokamak *Phys. Plasmas* **15** 056113
- [45] Kočan M *et al* 2008 Edge ion-to-electron temperature ratio in the Tore Supra tokamak *Plasma Phys. Control. Fusion* **50** 125009
- [46] Gunn J P *et al* 2007 Evidence for a poloidally localized enhancement of radial transport in the scrape-off layer of the Tore Supra tokamak *J. Nucl. Mater.* **363–365** 484–90
- [47] LaBombard B *et al* 2004 Transport-driven scrape-off-layer flows and the boundary conditions imposed at the magnetic separatrix in a tokamak plasma *Nucl. Fusion* **44** 1047
- [48] Kirnev G S *et al* 2005 EDGE2D code simulations of SOL flows and in-out divertor asymmetries in JET *J. Nucl. Mater.* **337–339** 271–5
- [49] Pitts R A *et al* 2005 Edge and divertor physics with reversed toroidal field in JET *J. Nucl. Mater.* **337–339** 146–53
- [50] Gallo A *et al* 2017 Impact of the plasma geometry on divertor power exhaust: experimental evidence from TCV and simulations with SolEdge2D and TOKAM3X *Plasma Phys. Control. Fusion* **60** 014007
- [51] Wensing M 2021 Drift-related transport and plasma-neutral interaction in the TCV divertor *PhD Thesis* EPFL (<https://doi.org/10.5075/epfl-thesis-8447>)
- [52] Eich T *et al* 2011 Inter-ELM power decay length for JET and ASDEX Upgrade: measurement and comparison with heuristic drift-based model *Phys. Rev. Lett.* **107** 215001
- [53] Casali L *et al* 2022 Impurity leakage and radiative cooling in the first nitrogen and neon seeding study in the closed DIII-D SAS configuration *Nucl. Fusion* **62** 026021
- [54] Meier E T *et al* 2017 Drifts, currents and power scrape-off width in SOLPS-ITER modeling of DIII-D *Nucl. Mater. Energy* **12** 973–7
- [55] Groth M *et al* 2013 Impact of carbon and tungsten as divertor materials on the scrape-off layer conditions in jet *Nucl. Fusion* **53** 093016
- [56] Chankin A V *et al* 2006 SOLPS modelling of ASDEX upgrade H-mode plasma *Plasma Phys. Control. Fusion* **48** 839
- [57] Christen N *et al* 2017 Exploring drift effects in TCV single-null plasmas with the UEDGE code *Plasma Phys. Control. Fusion* **59** 105004
- [58] Février O *et al* 2018 Analysis of wall-embedded langmuir probe signals in different conditions on the Tokamak α Configuration Variable *Rev. Sci. Instrum.* **89** 053502
- [59] De Oliveira H *et al* 2019 Langmuir probe electronics upgrade on the tokamak α configuration variable *Rev. Sci. Instrum.* **90** 083502
- [60] Theiler C *et al* 2017 Results from recent detachment experiments in alternative divertor configurations on TCV *Nucl. Fusion* **57** 072008
- [61] Niemczewski A 1995 Neutral particle dynamics in the Alcator C-Mod tokamak *PhD Thesis* MIT
- [62] Reimerdes H 2022 TCV experiments with divertor baffles *Invited Talk in the 25th Int. Conf. on Plasma Surface Interaction in Controlled Fusion Devices*
- [63] Pitts R A *et al* 2019 Physics basis for the first ITER tungsten divertor *Nucl. Mater. Energy* **20** 100696
- [64] Stangeby P C 2018 Basic physical processes and reduced models for plasma detachment *Plasma Phys. Control. Fusion* **60** 044022
- [65] Kallenbach A *et al* 2016 Analytical calculations for impurity seeded partially detached divertor conditions *Plasma Phys. Control. Fusion* **58** 045013
- [66] Eldon D *et al* 2021 An analysis of controlled detachment by seeding various impurity species in high performance scenarios on DIII-D and EAST *Nucl. Mater. Energy* **27** 100963
- [67] Kallenbach A and Henderson S 2022 personal communication
- [68] Loarte A *et al* 1999 Multi-machine scaling of the divertor peak heat flux and width for L-mode and H-mode discharges *J. Nucl. Mater.* **266–269** 587–92
- [69] Eich T *et al* 2013 Scaling of the tokamak near the scrape-off layer H-mode power width and implications for ITER *Nucl. Fusion* **53** 093031